



Minnesota State University, Mankato
Cornerstone: A Collection of Scholarly
and Creative Works for Minnesota
State University, Mankato

All Graduate Theses, Dissertations, and Other
Capstone Projects

Graduate Theses, Dissertations, and Other
Capstone Projects

2023

Development of a Permanent Magnet Spherical Motor with 3 Degrees of Freedom

Eric T. Hanson
Minnesota State University, Mankato

Follow this and additional works at: <https://cornerstone.lib.mnsu.edu/etds>

 Part of the [Mechanical Engineering Commons](#)

Recommended Citation

Hanson, E. T. (2023). Development of a permanent magnetic spherical motor with 3 degrees of freedom [Master's thesis, Minnesota State University, Mankato]. Cornerstone: A Collection of Scholarly and Creative Works for Minnesota State University, Mankato. <https://cornerstone.lib.mnsu.edu/etds/1301/>

This Thesis is brought to you for free and open access by the Graduate Theses, Dissertations, and Other Capstone Projects at Cornerstone: A Collection of Scholarly and Creative Works for Minnesota State University, Mankato. It has been accepted for inclusion in All Graduate Theses, Dissertations, and Other Capstone Projects by an authorized administrator of Cornerstone: A Collection of Scholarly and Creative Works for Minnesota State University, Mankato.

DEVELOPMENT OF A PERMANENT MAGNETIC SPHERICAL MOTOR WITH 3 DEGREES OF FREEDOM

This thesis is submitted in partial fulfillment of the requirements for the Degree of Master
of Science in Mechanical Engineering

Thesis By:

Eric T. Hanson

Thesis Adviser:

Dr. Min Li

Committee Members:

Dr. Pavan Karra

Dr. Vincent Winstead

Department of Mechanical and Civil Engineering

Minnesota State University, Mankato

Mankato, Minnesota

May, 2023

04/04/2023

Development of a Permanent Magnet Spherical Motor with 3 Degrees of Freedom

Eric T. Hanson

This thesis has been examined and approved by the following members of the student's committee.

Advisor: Dr. Min Li

Committee Member: Dr. Pavan Karra

Committee Member: Dr. Vincent Winstead

Acknowledgements

I would like to first express my sincerest thanks to my mentor and advisor, Dr. Min Li. Dr. Li has been an excellent educator in both my undergraduate and graduate studies and pushed me to pursue a master's degree. His guidance and support taught me how to research and how to learn, for without the completion of my thesis would not be possible.

It is also my pleasure to thank my committee members, Dr. Pavan Karra and Dr. Vincent Winstead. In addition to being great resources in completing my thesis, they both have made large contributions to my knowledge in control theory and have inspired me to keep learning more.

My decision to attend college and pursue a degree in STEM was mostly thanks to my high school trigonometry teacher, Mr. Kraig Pressler. Apart from being a great teacher, Mr. Pressler gave me confidence in myself as a student and as an individual that has allowed me to take on greater challenges in my life.

Also, I would like to thank Carson Giefer, Konner Brickey, and all the other undergraduate mechanical engineering students who have assisted me in developing the calibration module and training neural networks, while also making the long hours in lab more enjoyable.

I would finally like to acknowledge my parents, Scott and Jean Hanson, who have never given up on me and always encouraged me to be the best version of myself. The completion of my degree would not be possible without their constant support.

Table of Contents

Abstract	v
Chapter 1: Introduction and Background.....	1
1.1 Background	1
1.2 Previous and Recent Related Works.....	3
1.2.1 Spherical Motor Conception and Structures	3
1.2.2 Realtime Rotor Orientation Sensing	4
1.2.3 Modeling and Control	5
1.3 Thesis Outline	6
Chapter 2: Sensor Fusion Based Real-Time 3 DOFs Orientation Motion Estimation	7
2.1 Overall Sensing System Design.....	7
2.2 3 DOFs Orientation Estimation Based on Sensor Fusion.....	9
2.2.1 Orientation Sensing MFD Measurements.....	9
2.2.2 Angular Velocity Sensing EM Back-EMF Measurements	13
2.2.3 Sensor Fusion for Real-time Orientation Detection.....	15
Chapter 3: Real-Time 3 DOFs Orientation Motion Control Using Sliding Mode Method	17
3.1 Dynamic System Modeling.....	17
3.2 Real-Time 3 DOFs Orientation Motion Control.....	18
Chapter 4: Experimental Demonstration and Validation.....	22
4.1 Experimental Setup.....	22
4.2 Sensing Experiment Results and Analysis.....	27

4.3 Control Experimental Results and Analysis	34
4.3.1. Regulation Control.....	35
4.3.2 Tracking Control.....	38
Chapter 5: Concluding Remarks and Future Work.....	40
References.....	43
Appendix.....	46

DEVELOPMENT OF A PERMANENT MAGNETIC SPHERICAL MOTOR WITH 3 DEGREES OF FREEDOM

Eric T. Hanson

A Thesis Submitted in Partial Fulfillment of the Requirements for the Degree of Master
of Science in Mechanical Engineering

Minnesota State University, Mankato
Mankato, Minnesota

May, 2023

Abstract

This research is motivated by the need for actuators capable of delivering precise multiple degrees of freedom (DOF) motion with structure and energy efficiency in numerous applications. Permanent magnet spherical motors (PMSMs) are typical examples that can provide continuous and precise 3 dimensional (3D) rotational motion about a ball joint. The result of this research demonstrates a unique PMSM capable of 3D rotational motion control with high accuracy and bandwidth.

A Kalman filter (KF) sensor fusion method is developed to implement full state estimation of 3-DOF angular displacement and velocity in real time for a PMSM by simultaneously measuring the existing magnetic flux density (MFD) field and the back-electromotive-force (EMF) as inputs to the sensor fusion algorithm. More specifically, the bijective property between the orientation and measured MFD field is numerically demonstrated, which provides the basis to implement the measurement model through an artificial neural network (ANN) trained with a Levenberg-Marquardt algorithm. A mathematical model presenting the angular velocity and back-EMF measurements is formulated in quaternion representation, simplifying the computations required to implement the sensor fusion system while providing a reliable and accurate estimation of both the orientation and its angular velocity. The rotor dynamics are modeled and represented with time-varying nonlinear differential equations. The system uncertainties due to parameter inaccuracies of the cascaded system and the changes of the loads are analyzed. A sliding mode control (SMC) system is developed to precisely and robustly control the typical nonlinear system of the PMSM regardless of the system uncertainties. The capabilities of chatter suppression and error convergence of the proposed control law are investigated. A PMSM prototype fabricated using additive manufacturing is developed to experimentally demonstrate the facilitation of the motor design and effectiveness/accuracy of the entire 3D orientation feedback control system.

Chapter 1: Introduction and Background

1.1 Background

Modern advancements in robotics, manufacturing, and bio-medical engineering have provided a need for more sophisticated actuators. Wrist-like joints in robotic manipulators are often accomplished by grouping multiple 1 degree of freedom (DOF) motors into a single assembly. The result of which mimics 3-DOF rotation but is mechanically complex and cumbersome due to the multiple joints required and lacks swift dexterous motion required in modern applications. Spherical motors are researched as a solution to this problem, providing a method of 3-DOF rotation about a single joint.

The permanent magnet spherical motor (PMSM) is a novel type of multi-DOF actuator that has been widely researched. The general structure of a PMSM is that of a spherical rotor that rotates about a ball joint bearing. The rotor contains multiple permanent magnets (PMs) that interacts with an array of electrical magnet (EM) pairs embedded within the motor's stator. Manipulation of the rotor orientation is achieved by sending current to the EMs, inducing a magnetic torque between the EMs and PMs. As a unique current signal can be sent to each pair of EMs, the direction and magnitude of the provided torque can be altered. To better illustrate this, Figure 1 depicts the basic structure of a PMSM.

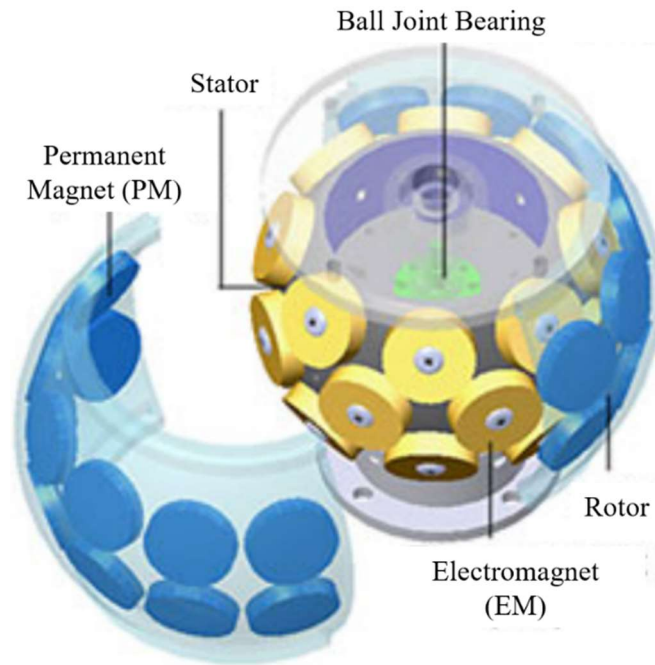


Fig. 1. CAD Model of PMSM Structure [1]

This research offers a unique PMSM design that solves the problem of non-uniqueness in magnetic field-based readings. A sensor fusion approach is also implemented for combining MFD (magnetic flux density) and back-EMF orientation readings using a Kalman Filter for improved state estimation. A sliding mode controller is then implemented for its ability to control nonlinear systems in presence of uncertainties. The finished product demonstrates capabilities of regulation and tracking control of the rotor's orientation with accurate sensing, which the research can then be applied to various applications requiring dexterous wrist-like motion.

1.2 Previous and Recent Related Works

This section details existing research organized into the following segments: an introduction into the different types of researched spherical motors, methods of real-time rotor orientation estimation, and finally electromagnetic system modeling and control strategies. A summary of the existing research is presented at the end of this section, highlighting key issues that this research aims to investigate.

1.2.1 Spherical Motor Conception and Structures

Research on spherical motors began with the spherical induction motor, designed, and developed by Laithwaite *et al.* [2-4] in the late 1950s and early 1960s. Other methods of obtaining 3-DOF spherical actuation have been developed, including variable reluctance (VR) [5-7], stepper [8, 9], direct current [10, 11], and ultrasonic [12, 13] spherical motors.

Of the different types of spherical motors, most operate on the principle of electromagnetism. The spherical induction motors are similar to single-DOF induction motors, in which dynamic current signals are sent through three-phase windings of the stator, whose magnetic field induces an EMF in the rotor. The EMF of the rotor also generates a magnetic field which generates a torque when interacting with the magnetic field of the stator. Although research has proven the validity of these motors, the design is inherently complex due to the multi-DOF three phase winding configurations and laminations are necessary to prevent unwanted eddy currents, encouraging research into more practical designs.

1.2.2 Realtime Rotor Orientation Sensing

Orientation sensing is a crucial element in controlling a PMSM. A variety of different methods have been researched to describe the orientation of a PMSM. In [5, 6, 9], an encoder system is designed to track the angle of an output shaft attached to a rotor. The result of which provides a method of tracking rotor orientation with high determinism, but its large size can be detrimental in modern applications that require space efficient joints.

This requirement encourages sensor less or contact-free sensing methods. In [14-16], vision/optical systems have been implemented as a means of contact-free sensing. These systems look for patterns on the surface of the rotor to determine their orientation. Vision systems are often computational intense and require the surface of rotor to be manufactured with a specific pattern required for the vision system to detect orientation.

The magnetic fields produced by PMSM systems have been utilized for contactless sensing. In [17-19], an array of MFD sensors are used to measure the existing PMSM's magnetic field and use an artificial neural network (ANN) to map the relationships between MFD sensor readings to the rotor's orientation. Symmetry in a PMSM's design results in the absence of the bijective property between measured MFD and rotor orientation. This means that there are multiple possible orientations that result in the same magnetic field, also known as the "magnetic inverse" problem. In [18], this problem is solved by splitting the rotors orientation into multiple connected bijective domains and developing a method to identify which domain the rotor is currently in but increases the complexity of the system.

The motion of the PMs embedded within the rotor results in a changing magnetic flux within the EMs that then induces a back-EMF. In [20-22], the back-EMF measured in the coils of the EMs are measured as a means of sensor-free orientation methods, which produces an expression for the rotor's angular velocity. This result can then be integrated to approximate the rotor orientation but is only accurate with a well-defined model and is still subject to sensor drift, similar to an inertial measurement unit (IMU).

1.2.3 Modeling and Control

Spherical motors are highly nonlinear systems, making them difficult to both model and control. In particular, determining the force/torque generated from the interaction between PMs and EMs is computationally intensive. The Lorentz force equation and the Maxwell stress tensor are commonly used methods to describe the attractive and repulsive forces between magnets [6, 23, 24]. In [25], a dipole model is used to obtain a closed form solution for calculating magnetic field values of PMs and EMs. [1] expands on this and characterizes EMs as equivalent PMs and uses the dipole model for a closed-form solution of the torque model between PM and EMs in real-time.

Given the complexity of the PMSM model, non-linear control schemes are often utilized to achieve regulation and tracking control. Modeled and unmodeled uncertainties along with disturbances have a significant impact on a controller's performance, requiring that the controller needs to also be robust. In [26], a neural network is trained to compensate for uncertainties in a PMSM model in combination with a fuzzy logic controller to achieve effective continuous trajectory control. In [18], a relationship between orientation and corresponding field values are used to create a magnet field-

based PD controller to determine the desired torque, followed by a nonlinear inverse torque model to determine the appropriate control signal to send to the EMs. A terminal sliding mode control is applied to a PMSM on a sliding motion stage in [27] for feed-forward compensation of modeling uncertainties resulting in an average tracking error of less than 0.07° .

1.3 Thesis Outline

The remainder of this thesis is organized into the following chapters. Chapter 2 introduces the basic design of the PMSM created for this research and details the sensing methods used for real time orientation estimation. This includes an ANN model that estimates orientation from MFD measurements, rotor angular velocity from EM back-EMF measurements, and sensor fusion using Kalman Filter for improved state estimation. Chapter 3 explains the nonlinear control of the PMSM, for which a SMC (sliding mode control) algorithm is derived considering the dynamic system model. Chapter 4 presents experimental results demonstrating the sensing and control system capabilities. Chapter 5 provides a conclusion to the results of the research, as well as comments on future work as a continuation of this research.

Chapter 2: Sensor Fusion Based Real-Time 3 DOFs

Orientation Motion Estimation

2.1 Overall Sensing System Design

Figure 2 illustrates a 3-DOF PMSM (a-c) with a weight compensating regulator (WCR) along with block diagram representations of the proposed control (d) and sensing (e) scheme. The motor's stator is a ball-like shape housing N_E EMs embedded on its outer surface. The rotor is a spherical shell containing N_P spherically aligned cylindrical PMs and is supported by a spherical roller bearing mounted at the center of the stator. The WCR is made up of an upper and lower ring of N_W evenly spaced cylindrical PMs which are separately attached to the rotor and stator. The direction of the poles of the PMs in each ring are opposite to support the weight of rotor through magnetic repulsion. In between the rings of the WCR, is a circular ring of N_S evenly spaced single-axis Hall effect sensors embedded in the stator that measure the vertical component of MFD at each sensor's respective location.

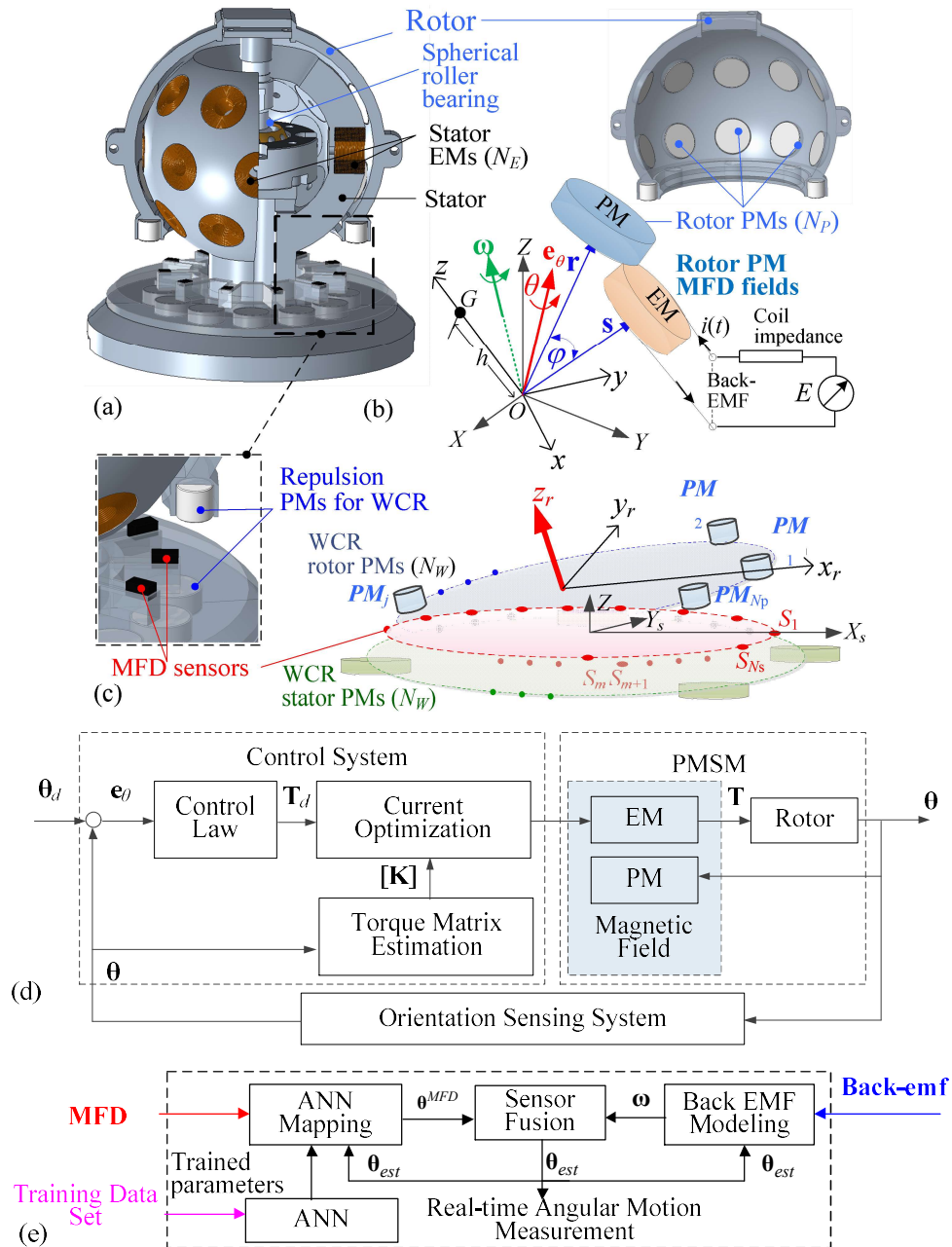


Fig. 2. 3-DOF spherical actuator system. (a) PMSM, (b) Back-EMF measurements, (c) WCR with MFD sensors, (d) Block diagram of PMSM system, (e) Flowchart of orientation sensing system.

The reference XYZ coordinate system of the stator and the moving xyz coordinate system of the rotor share a common origin defined at the center of the spherical roller

bearing which the rotor is free to rotate about. The rotor orientation can be described using an equivalent angle-axis $\boldsymbol{\theta} = [\theta_x \ \theta_y \ \theta_z]$ with spin angle $\theta (= |\boldsymbol{\theta}|)$. The WCR coordinate systems are defined as $X_S Y_S Z_S$ and $x_r y_r z_r$ corresponding to the stator and rotor WCR PM rings, respectively. The stator- XY plane and rotor- xy plane is parallel to the $X_S Y_S$ and $x_r y_r$ planes respectively, where the X_S and x_r axes are pointing in the direction of S_1 and PM_1 , and the Z_S and z_r align with the Z and z axes, respectively.

2.2 3 DOFs Orientation Estimation Based on Sensor Fusion

Information regarding the orientation of the rotor can be predicted using two separate measurements: the back-EMF induced in the EMs by the moving PMs and the MFD produced from the WCR measured by the Hall effect sensors. As each method can estimate orientation individually, a Kalman Filter can be implemented to fuse the two measurements together to increase the accuracy of the orientation estimation.

2.2.1 Orientation Sensing MFD Measurements

The WCR consists of a ring of PMs located on the rotor and the stator that repel each other. The WCR ring of the stator is made up of N_W cylindrical PMs that are assumed to be identical in geometry and magnetization, where the ring of the rotor also has N_W cylindrical PMs but each with unique magnetic strengths. Located between the pair of PM-rings, is a ring of N_S ($\neq N_W$) evenly spaced single-axis MFD sensors. Each MFD sensor is oriented to detect the Z -component of $[\mathbf{B}_S]$ at the respective sensor location, where the set of all MFD readings can be defined by the vector \mathbf{B} with length N_S .

Given that $\mathbf{B} = \mathbf{B}(\boldsymbol{\theta})$ and a unique \mathbf{B} exists for the entire domain of $\boldsymbol{\theta}$, an ANN can be trained to map the sensor readings to a corresponding rotor orientation. If this uniqueness exists, it is said that the bijective property exists between \mathbf{B} and $\boldsymbol{\theta}$. This is possible when each magnet in the rotor WCR ring is unique, as if the magnets were identical, the value of $\mathbf{B}(\boldsymbol{\theta})$ given a rotor inclination \mathbf{e}_z would be identical to $\mathbf{B}(\boldsymbol{\theta} + 2\pi \cdot i/N_w)$ where i can be any integer as the magnets are evenly distributed. When the magnets have unique strengths, it acts as a signature that the set of MFD sensors can detect. Given that a unique \mathbf{B} exist for any possible rotor orientation, an ANN can be used to output orientation given the MFD readings as an input.

To guarantee that the bijective property between $\boldsymbol{\theta}$ and $\mathbf{B}(\boldsymbol{\theta})$ exists, the measurement vectors \mathbf{B} at any two different spin angles, θ_1 and $\theta_2 (\neq \theta_1)$ are distinct. This can be expressed mathematically, shown in Equation (1).

$$\forall 0 \leq \theta_1, \theta_2 < 2\pi, \mathbf{B}(\theta_1) \neq \mathbf{B}(\theta_2 \neq \theta_1) \quad (1)$$

Considering the m^{th} sensor, $\Delta B_m = B_m(\theta_1) - B_m(\theta_2)$. Expanding on this expression using the Fourier series results in Equations (2a ,b)

$$\Delta B_m = \sum_{k=1}^{\infty} a_{mk} (\cos \phi_{m1} - \cos \phi_{m2}) \quad (2a)$$

$$\text{where } \begin{bmatrix} \phi_{m1} \\ \phi_{m2} \end{bmatrix} = kn_w \begin{bmatrix} \theta_1 + 2\pi(m-1)/N_s \\ \theta_2 + 2\pi(m-1)/N_s \end{bmatrix} \quad (2b)$$

From this, it can be seen that $\Delta \mathbf{B} = \mathbf{0}$ only when $\phi_{m1} + \phi_{m2} = (2l + 1)\pi$ or $\phi_{m2} = \phi_{m1} + 2l\pi$ (where l is an arbitrary integer) for all possible k and m . In other words, $\Delta \mathbf{B} = \mathbf{0}$ only when Equation (3) shown below is satisfied.

$$\theta_1 + \theta_2 = \frac{(2l + 1)\pi}{n_w k} - \frac{4(m - 1)\pi}{N_s} \quad (3a)$$

$$\theta_1 - \theta_2 = 2\pi \frac{l}{n_w k} \quad (3b)$$

Given θ_1 and θ_2 in the range $[0, 2\pi)$, it is impossible to find the values of θ_1 and θ_2 to satisfy (5a) for all $m=1, \dots, N_s$. Meanwhile, since $0 < |\theta_1 - \theta_2| < 2\pi$, $0 < |l/(n_w k)| < 1$ from (5b) which is valid only when $n_w > 1$ for all positive integer k . Thereby, the bijective property between θ and $\mathbf{B}(\theta)$ exists when the WCR rotor PMs are distinct.

The magnetic orientation sensing method is best illustrated numerically with the aid of Figure 3(a) shown in the following page where \mathbf{P} is the intersection point between \mathbf{e}_z and the plane $Z = 1$ in the XYZ coordinate system expressed in Equation (4).

$$\mathbf{e}_z = \frac{\mathbf{P}}{|\mathbf{P}|}, \text{ where } \mathbf{P} = [X_p \quad Y_p \quad 1]^T \quad (4)$$

The magnetic fields of the WCR PMs are simulated using a commercial COMSOL finite element analysis (FEA) software. The values of the WCR and sensor parameters (defined in Figs. 2c and 3a) used in the FEA are summarized in Table 1. Operated in repulsion, all PMs are axially magnetized; the lower-ring PMs are assumed to be identical and N_s ($= 11$ or $N_w - 1$) sensors are single-axis measuring the $B = B_z$ component. Figures 3(b) and 3(c, d) are typical results revealing the effects of the spin-angle θ and inclination \mathbf{e}_z on the measured B by S_l and (S_l, S_4) , respectively. Figure 3(b) simulates “sensor S_l measurements” as θ spins from 0° to 360° while the inclination \mathbf{e}_z is maintained at $\mathbf{P} = [-0.1 \ 0.1 \ 1]$ for two upper-ring designs; identical PMs (top) and non-

uniform PM layout (bottom). The effects of the upper-ring-PM designs on the simulated B can be analyzed by the two plots in Figure 3(b). As shown in the upper plot that assumes identical upper-ring PMs, $n_w = N_w$. Using a non-uniform PM layout (bottom plot), $n_w = 1$ ensures that the bijective property between θ and $\mathbf{B}(\theta)$ exists.

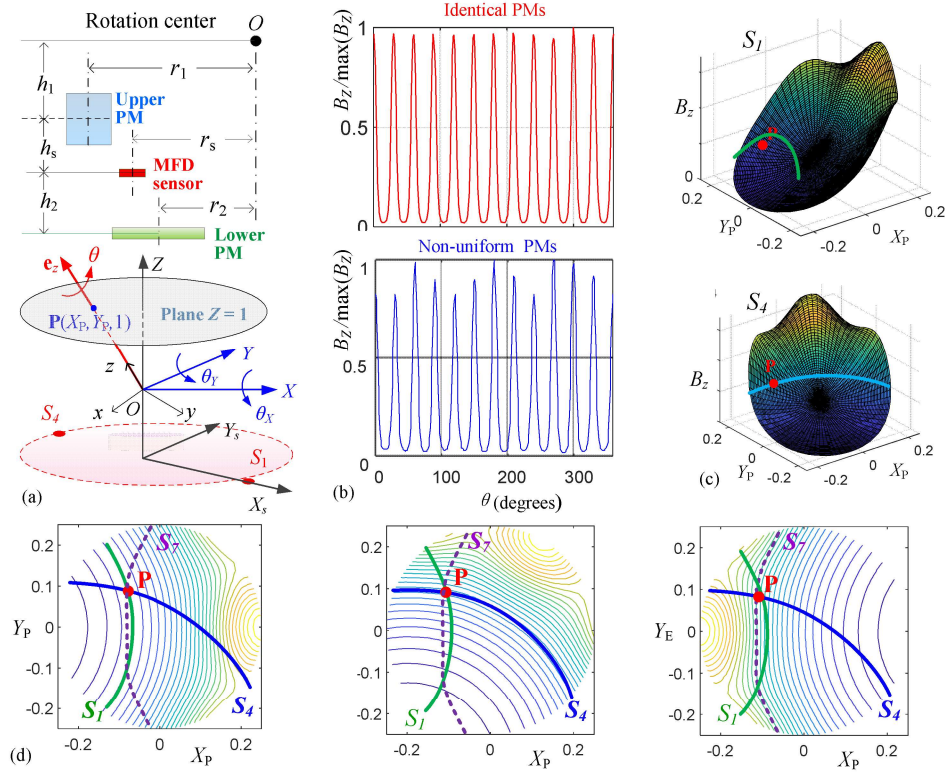


Fig. 3. Schematics illustrating the bijective properties of the orientation sensing method. (a) Coordinates and parametric values used in FEA. (b) Comparison of simulated B at S_1 when θ changes from 0° to 360° at $\mathbf{P} = [-0.1 \ 0.1 \ 1]$: Identical PMs (top). Non-uniform layout (bottom). (c) MFD fields measured by Sensors S_1 and S_4 . (d) Isolines (S_1 , S_4 , S_7) for estimating the shaft inclination.

Table 1. COMSOL Simulation Parameters

WCR ($N_w = 12$): $h_1 = 51, h_2 = 13, r_1 = 47, r_2 = 35$.	
Lower-ring PM : Diameter $d_o = 10$, Length $l_p = 9.8, \mu_0 M = 0.1732\text{T}$	
Upper-ring PM : $d_o = 20, l_p = 2$.	
Identical $\mu_0 M$	Three different types of PMs : $\mu_0 M$ (Location index)
$\mu_0 M(\text{T})$	0.244T (1,5,9,10), 0.229T (2,4,8,12), 0.203T (3,6,7,11)
MFD sensors ($N_s = 11$): $h_s = 15, r_s = 38$, S_1 and S_4 are used	

Figure 3(c) simulates the “ B fields measured by the two sensors (S_1, S_4)” over all possible locations of \mathbf{P} on the $Z=1$ plane by tilting the shaft at a specified $\theta = 0^\circ$. The corresponding (S_1, S_4) isolines or the constant B contours are shown in the (left, middle) plots of Figure 3(d). Similarly, the right plot of Figure 3(d) shows the isolines measured by S_7 . The isolines are mostly arc-shaped and well-defined illustrating that three single-axis sensors are sufficient to uniquely determine the unit-normal \mathbf{e}_z as revealed in Figure 3(d) where three unique (S_1, S_4, S_7) isolines intersect $Z=1$ plane at \mathbf{P} (solid-red circle).

2.2.2 Angular Velocity Sensing EM Back-EMF Measurements

The motion of the embedded PMs within the rotor will induce a voltage in the stator’s EM. The value of this voltage carries information relating to the angular velocity of the rotor. Considering one EM and PM pair, the moving magnetic field of the PM induces a back-EMF that can be expressed as time derivative of magnetic flux linkage Λ_p . This can be found by subtracting the voltage over the coil impedance from the measured voltage E which current i flows through with self-inductance L :

$$\frac{d\Lambda_p}{dt} = E - \left(R_e i + L \frac{di}{dt} \right) \quad \text{where } \Lambda_p = f(\varphi) \quad (5a, b)$$

It is denoted above that the magnetic flux linkage between an EM and PM is a function of the separation angle $\varphi (= \cos^{-1}(\mathbf{e}_r \cdot \mathbf{e}_s))$ between the two and PM polarity $\lambda (= 1, -1)$. Taking the time derivative of Equation (5b) and equating it to Equation (5a) results in Equation (6) shown below.

$$E - \left(Ri + L \frac{di}{dt} \right) = f'(\varphi) \lambda \cdot \frac{\dot{\mathbf{e}}_r \cdot \mathbf{e}_s}{\sqrt{1 - (\mathbf{e}_r \cdot \mathbf{e}_s)^2}} \quad \text{where } f'(\varphi) = \frac{df(\varphi)}{d\varphi} \quad (6a, b)$$

Expanding (6a) to account for the contributions from all N_E EMs and N_P PMs, the back-EMF in the j_{th} EM due to the angular velocity $\boldsymbol{\omega}$ can be expressed using Equation (7).

$$\mathbf{G}_j \boldsymbol{\omega} = E_j - \left(\mathbf{L}_j \frac{d\mathbf{I}_s}{dt} + R_j i_j \right) \quad \text{where } \mathbf{G}_j = \sum_{i=1}^{N_p} \frac{-\lambda_i (\mathbf{e}_{ri} \times \mathbf{e}_{sj})^T f'(\varphi_{ij})}{\sqrt{1 - (\mathbf{e}_{ri} \cdot \mathbf{e}_{sj})^2}} \quad (7a, b)$$

$$\mathbf{L}_j = [L_{1j} \dots L_{nj} \dots L_{N_E j}] \quad \text{and } \mathbf{I}_s(t) = [i_1(t) \dots i_j(t) \dots i_{N_E}(t)]^T \quad (7c, d)$$

Here, $\boldsymbol{\omega}$ represents the angular velocity of the rotor from $\dot{\mathbf{e}}_r$ and \mathbf{G}_j is a row vector derived from (6a) considering the effects of all i PMs on the j_{th} EM. \mathbf{L}_j is the j_{th} EM inductance vector where L_{nj} is the EM's self-inductance ($n = j$) and mutual inductances ($n \neq j$) between the n_{th} and j_{th} EM.

Considering each EM, a set of N_E linear equations can be expressed in matrix form shown in Equation (8a). Here, \mathbf{Y} is a column vector corresponding to set of back-EMF calculations shown in (8b).

$$[\mathbf{G}] \boldsymbol{\omega} = \mathbf{Y} \quad \text{where } \mathbf{Y} = \mathbf{E} - \left([\mathbf{L}] \frac{d\mathbf{I}_s}{dt} + R_e \mathbf{I}_s \right) \quad (8a, b)$$

$$[\mathbf{G}] = [\mathbf{G}_1 \dots \mathbf{G}_j \dots \mathbf{G}_{N_E}]^T \quad \text{and } [\mathbf{L}] = [\mathbf{L}_1 \dots \mathbf{L}_j \dots \mathbf{L}_{N_E}]^T \quad (8c, d)$$

So long as N_E is 3 or greater, $\boldsymbol{\omega}$ can be estimated by using the least square method shown in Equation (9).

$$\boldsymbol{\omega} = ([\mathbf{G}]^T[\mathbf{G}])^{-1}[\mathbf{G}]^T\mathbf{Y} \quad (9)$$

2.2.3 Sensor Fusion for Real-time Orientation Detection

The measurement outputs from the ANN and the EM back-EMF can be combined using a KF to improve orientation estimation accuracy while incorporating unmodeled factors. The output of the ANN and the back-EMF can be expressed in quaternion form.

$$\mathbf{q} = ANN(\mathbf{B}) \text{ where } \mathbf{q} = \left[\cos\left(\frac{\theta}{2}\right) \mathbf{e}_\theta \sin\left(\frac{\theta}{2}\right) \right] \text{ and } \|\mathbf{q}\| = 1 \quad (10a, b, c)$$

The advantage of using quaternion representation compared to rotation matrices is that the number of computations required for 4-dimensional number operations is far less than that which is required for 3x3 matrix multiplications.

Expressing the rotor angular velocity in quaternion form, $\boldsymbol{\omega}_q = [0 \ \boldsymbol{\omega}]$, the time derivative of \mathbf{q} can be solved using Equation (11a) and rewritten for discrete KF implementation [29] in Equation (11b), where \otimes is the Hamilton product operation.

$$\dot{\mathbf{q}} = \frac{1}{2} \mathbf{q} \otimes \boldsymbol{\omega}_q \text{ and } \dot{\mathbf{q}}_k = \frac{1}{2} \hat{\mathbf{q}}_{k-1} \otimes \boldsymbol{\omega}_{qk} \quad (11a, b)$$

The subscripts k and $k - 1$ in Equation (11b) refer to the discrete measurements at time $t = kT$ and previous time step $t = (k - 1)T$.

The discrete KF state space model can be expressed as follows, where the estimated state and control-input vectors are defined in Equation (12a, b), the KF state space model is shown (8c), and the KF output is expressed in (12d) [30].

$$\hat{\mathbf{x}}_k = [\hat{\mathbf{q}}_k \ \hat{\mathbf{q}}_{bk}]^T; \ \mathbf{u}_k = \dot{\mathbf{q}}_k \quad (12a, b)$$

$$\mathbf{x}_k = \begin{bmatrix} [I] & -T[I] \\ \mathbf{0} & [I] \end{bmatrix} \mathbf{x}_{k-1} + \begin{bmatrix} T[I] \\ \mathbf{0} \end{bmatrix} \mathbf{u}_k + \mathbf{w}_k \quad (12c)$$

$$\mathbf{z}_k = [\mathbf{1} \ \mathbf{0}] \mathbf{x}_k + \mathbf{v}_k \quad (12d)$$

Here, \mathbf{w}_k and \mathbf{z}_k represent the process and measurement noise, respectively. The initial state and measurement error covariance matrices necessary to implement the KF algorithm can be estimated from experimental results and further tuned to improve the accuracy of the model. The KF sensing algorithm is illustrated in block diagram form in Figure 4.

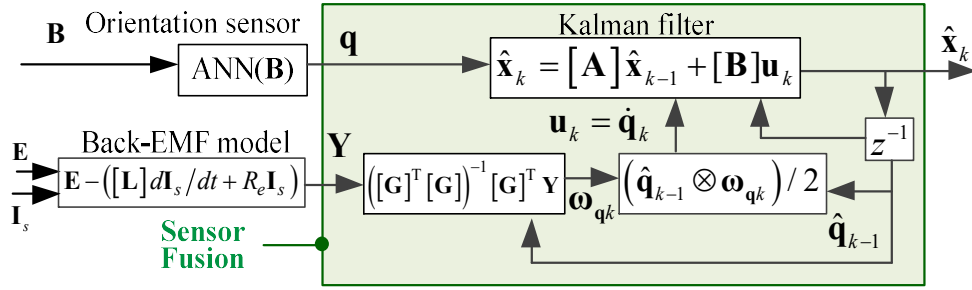


Fig. 4. Flowchart illustrating sensor fusion for orientation estimation.

Chapter 3: Real-Time 3 DOFs Orientation Motion Control

Using Sliding Mode Method

After the development of the orientation sensing system, a control algorithm can be implemented to drive the rotor to a desired state. The current supplied to the array of EM pairs is the control signal, \mathbf{u} , as the resulting magnetic field induces a torque that interacts with the magnetic field of the PMs. Given the nonlinearity of the system, a SMC algorithm can be used to account for these nonlinearities as well as modeled and unmodeled uncertainties.

3.1 Dynamic System Modeling

Given the symmetry of the system, the rotor's rotational mass J can be expressed as a diagonal matrix. The sum of torques at the systems origin is expressed below in Equation (13).

$$\sum \mathbf{T}_0 = \mathbf{T}_u - \mathbf{T}_r = \frac{d\mathbf{H}_0}{dt} = \frac{\partial \mathbf{H}_0}{\partial t} + \boldsymbol{\omega} \times \mathbf{H}_0 \quad (13a, b, c)$$

$$\text{where } \mathbf{T}_r = \mathbf{T}_g + \mathbf{T}_{WCR} \text{ and } \mathbf{T}_u = [\mathbf{K}_T]\mathbf{u}$$

Equation (9a) expresses the net torque applied to the rotor in the stator coordinate system, which can be expressed as the time derivative of angular momentum, $\mathbf{H}_0 (= J\boldsymbol{\omega})$. \mathbf{T}_u is the control torque generated as a result of current, \mathbf{u} , flowing through the EMs and \mathbf{T}_r is the restorative torque \mathbf{T}_r , consisting of the torque created due to gravity, \mathbf{T}_g , and the repulsive torque of the WCR, \mathbf{T}_{WCR} . Both terms in \mathbf{T}_r are orientation dependent, where \mathbf{T}_g can be directly calculated given $\boldsymbol{\theta}$ and \mathbf{T}_{WCR} can be calculated through simulation.

The control torque gain, $[\mathbf{K}_T]$, is a $3 \times N_E$ matrix, whose elements are also orientation dependent, determines the direction and magnitude of torque generated from every EM at a given instance. $[\mathbf{K}_T]$ can be calculated for a given orientation using the Lorentz Force Law (A.1).

Substituting $\mathbf{H}_0 = [\mathbf{J}]\boldsymbol{\omega}$ and Equation (13c) Equation (13a) results in the following expression.

$$[\mathbf{J}]\ddot{\boldsymbol{\theta}} + [\text{skew}(\dot{\boldsymbol{\theta}})][\mathbf{J}]\dot{\boldsymbol{\theta}} + \mathbf{T}_r = [\mathbf{K}_T]\mathbf{u} \quad (14)$$

To account for the model uncertainty in developing the control algorithm for the non-linear dynamics, the terms \mathbf{J} , $[\mathbf{K}_T]$, and \mathbf{T}_r can be separated into nominal terms denoted by the subscript '0' and an uncertain deviation Δ from the nominal term, which are expressed in (15a, b, c)

$$[\mathbf{J}] = [\mathbf{J}_0] + [\Delta\mathbf{J}], \quad [\mathbf{K}_T] = [\mathbf{K}_{T0}] + [\Delta\mathbf{K}_T], \quad \mathbf{T}_r = \mathbf{T}_{r0} + \Delta\mathbf{T}_r \quad (15a, b, c)$$

Distributing these expressions into (14) and separating nominal and uncertain terms into separate equations results in the system dynamics shown below in Equations (16a) with disturbance term in (16b).

$$[\mathbf{J}_0]\ddot{\boldsymbol{\theta}} + [\text{skew}(\dot{\boldsymbol{\theta}})][\mathbf{J}_0]\dot{\boldsymbol{\theta}} + \mathbf{T}_{r0} + \mathbf{D} = [\mathbf{K}_{T0}]\mathbf{u} \quad (16a)$$

$$\mathbf{D} = [\Delta\mathbf{J}]\ddot{\boldsymbol{\theta}} + [\text{skew}(\dot{\boldsymbol{\theta}})][\Delta\mathbf{J}]\dot{\boldsymbol{\theta}} + \Delta\mathbf{T}_r - [\Delta\mathbf{K}_T]\mathbf{u} + \mathbf{d} \quad (16b)$$

Here, \mathbf{D} represents the total uncertainty where \mathbf{d} represents the unmodeled uncertainty.

3.2 Real-Time 3 DOFs Orientation Motion Control

To account for the number of modeled and unmodeled uncertainties, a SMC algorithm is proposed. SMC takes into consideration the nonlinearity of the system while also being robust. The 1st order sliding surface is defined in Equation (17).

$$\mathbf{s} = \left(\frac{d}{dt} + [\mathbf{P}] \right)^k \mathbf{e} \text{ where } \mathbf{e} = \boldsymbol{\theta}_d - \boldsymbol{\theta} \quad (17a, b)$$

$$k = r - 1; \text{ and } [\mathbf{P}] = \mathbf{diag}(P_1 \ P_2 \ P_3) \quad (17c, d)$$

Here, r represents the order of the system which can be seen from the system dynamics in Equation (16a) to be equal to 2, and P_i are positive constants. Substituting $k = 1$ into Equation (17a) results in the following sliding surface followed by its derivative.

$$\mathbf{s} = \dot{\mathbf{e}} + [\mathbf{P}]\mathbf{e} \text{ and } \dot{\mathbf{s}} = \ddot{\boldsymbol{\theta}}_d - \ddot{\boldsymbol{\theta}} + [\mathbf{P}]\dot{\mathbf{e}} \quad (18a, b)$$

Solving Equation (16a) for $\ddot{\boldsymbol{\theta}}$ and substituting the results into Equation (17b) results into the following expression.

$$\dot{\mathbf{s}} = \ddot{\boldsymbol{\theta}}_d + [\mathbf{P}]\dot{\mathbf{e}} + [\mathbf{J}_0]^{-1}([\mathit{skew}(\dot{\boldsymbol{\theta}})][\mathbf{J}_0]\dot{\boldsymbol{\theta}} + \mathbf{T}_{r0} + \mathbf{D} - [\mathbf{K}_{T0}]\mathbf{u}) \quad (19)$$

By maintaining the sliding surface to $\mathbf{s} = \mathbf{0}$, the error dynamics will converge to 0 as (18a) becomes $\dot{\mathbf{e}} = -[\mathbf{P}]\mathbf{e}$. When $\mathbf{s} \neq \mathbf{0}$, a control input should be applied that the sliding dynamics in (18) ensures that $\mathit{sgn}(\mathbf{s}) = -\mathit{sgn}(\dot{\mathbf{s}})$. The control effort can then be described as the combination of maintaining $\mathbf{s} = \mathbf{0}$ and coercing $\dot{\mathbf{s}}$ when $\mathbf{s} \neq \mathbf{0}$.

Therefore, we can express the total control effort as the following.

$$\mathbf{u} = \mathbf{u}_{eq} + \mathbf{u}_{sw} \quad (20)$$

Here, \mathbf{u}_{eq} and \mathbf{u}_{sw} are the equivalent and switching control, respectively. The former term provides the main control action assuming that $\mathbf{D} = \mathbf{0}$ that maintains $\dot{\mathbf{s}} = \mathbf{0}$, where the latter term provides addition control effort for the uncertainties and disturbances while also adjusting the sliding dynamics when the system is not on the sliding surface, both of which are expressed in (21a) and (22b).

$$\mathbf{u}_{eq} = [\mathbf{K}_{T0}]^{-1} \left([\mathbf{J}_0] (\ddot{\boldsymbol{\theta}}_d + [\mathbf{P}] \dot{\mathbf{e}}) + skew(\dot{\boldsymbol{\theta}}) [\mathbf{J}_0] \dot{\boldsymbol{\theta}} + \mathbf{T}_{r0}(\boldsymbol{\theta}) \right) \quad (21a)$$

$$\mathbf{u}_{sw} = [\mathbf{K}_{T0}]^{-1} [\mathbf{J}_0] [\mathbf{k}] sgn(\mathbf{s}) \quad (21b)$$

In (21b), $[\mathbf{k}]$ represents a diagonal matrix whose diagonal components are positive constants. The choosing of $[\mathbf{k}]$ and $[\mathbf{P}]$ can be tuned to enhance desired performance.

The algorithm necessary to compute the control law can be better visualized in block diagram form, shown below in Figure 5.

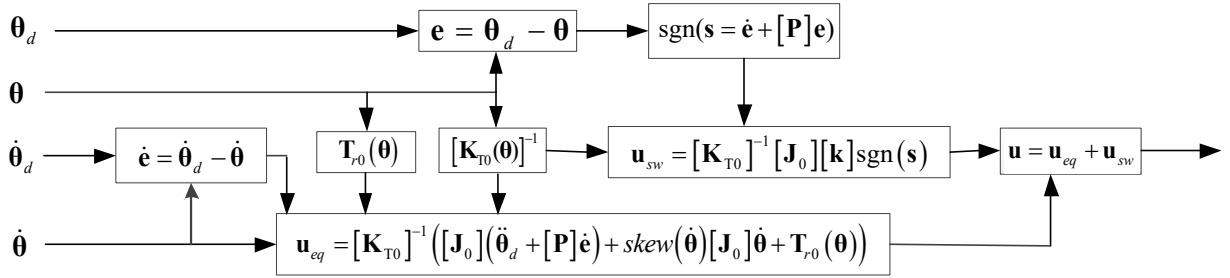


Fig. 5. Control law algorithm depicted in block diagram form.

To reduce the chatter introduced by the switching function in (21b), the sign function can be approximated as a hyperbolic tangent smoothing function with smoothing constant, Ω , expressed in Equation (22).

$$sign(\mathbf{s}) \approx \tanh\left(\frac{\mathbf{s}}{\Omega}\right) \quad (22)$$

The utility of using the smoothing function is that the switching control effort decreases as \mathbf{s} approaches $\mathbf{0}$, whereas without the smoothing function the switching control would be of constant magnitude unless \mathbf{s} is exactly $\mathbf{0}$. The smoothing constant, Ω , can be tuned to adjust the amount of smoothing, where the hyperbolic tangent function more similarly resembles the sign function as Ω approaches 0.

The system's stability is analyzed using the Direct Lyapunov stability method, where the Lyapunov function is expressed in Equation (23) where $V = 0$ when $\mathbf{s} = \mathbf{0}$ and $V > 0$ when $\mathbf{s} \neq \mathbf{0}$.

$$V = \mathbf{s}^T \mathbf{s} / 2 \quad (23)$$

The error of the trajectory of sliding dynamics from the reaching phase to the sliding phase can converge under the following condition.

$\dot{V} < 0$ when $\mathbf{s} \neq \mathbf{0}$ where

$$\begin{aligned} \dot{V} = \mathbf{s}^T \dot{\mathbf{s}} = \mathbf{s}^T \left([\mathbf{J}_0]^{-1} \mathbf{D} - [\mathbf{k}] \text{sgn}(\mathbf{s}) \right) &= \begin{bmatrix} D_1 & D_2 & D_3 \end{bmatrix} \mathbf{s} - [k_1 \quad k_2 \quad k_3] |\mathbf{s}| \\ &< - \left[\left(k_1 - \frac{D_{max1}}{J_1} \right) \quad \left(k_2 - \frac{D_{max2}}{J_2} \right) \quad \left(k_3 - \frac{D_{max3}}{J_3} \right) \right] |\mathbf{s}| \end{aligned} \quad (24)$$

where $[D_{max1} \ D_{max2} \ D_{max3}]^T = \max(\mathbf{D})$. The stability condition in the previous expression will be satisfied when $k_i < D_{maxi}/J_i$.

Chapter 4: Experimental Demonstration and Validation

The prototype system of the permanent magnetic spherical motor is validated through a series of experiments. First, the overall structure and components of the prototype system is introduced. A training module is developed to automatize the data collection required for training the ANN model. The sensing system is then evaluated through comparison of ground truth orientation measurements to the orientation output of the real time sensing system. After validation of the PMSM's sensing capabilities, the SMC is implemented in the prototype system, testing its regulation and tracking capabilities. The first section of this chapter details the experiments and corresponding results validating the sensing system, followed by a section experimentally validating the control system and the overall PMSM design.

4.1 Experimental Setup

The mechanical structures of the spherical motor with weight-compensation are 3D-printed with PLA plastic filament based on the design presented in Figure 2. Figure 6 shown on the next page depicts the experimental hardware used for the experiments in this chapter. Supported on a spherical roller bearing (SRJ012C), the rotor is capable of full ($0^{\circ}\sim 360^{\circ}$) spin about the shaft that has an inclination range of $\pm 12^{\circ}$ tilt angle. An optical system consisting of two orthogonal laser-pointers and an inertial measurement unit (IMU with Model No. MPU6050) as shown in Figure 6(c) are placed on the top of the rotor to obtain data for the ANN training and prototype evaluation/demonstration purposes. The parameters of the weight compensation and magnetic sensing systems are listed in Table 2 whereas the parameters of rotor PMs and stator EMs of the spherical

motor are tabulated in Table 3. The stator EMs are custom-manufactured on a coil-winding machine and fabricated with the same copper wire and the same number of turns. The resistances of all the EMs are measured within the range $(11 \pm 0.13) \Omega$.

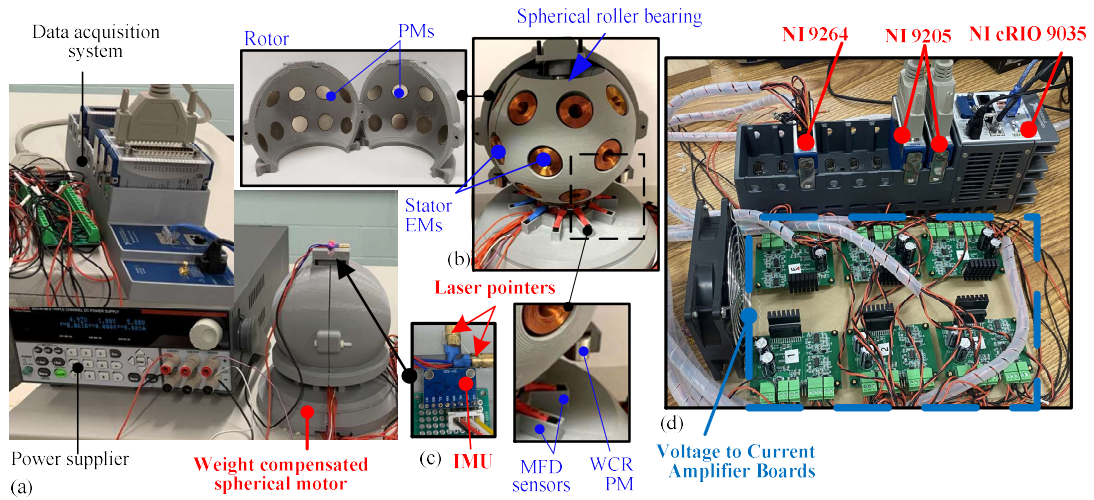
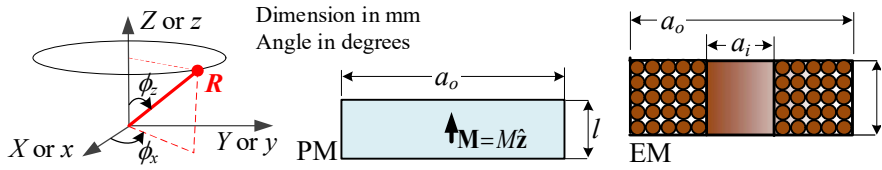


Fig. 6. Experimental testbed. (a) Overview. (b) Prototype spherical motor. (c) Embedded sensors and sensing systems for verification. (d) Controller with IO modules and current amplifier boards.

Table 2. Parameters used in the simulations (Dimension in mm).

WCR ($N_w = 12$): $h_1 = 51, h_2 = 13, r_1 = 47, r_2 = 35$.	
Lower-ring PM : Diameter $d_o = 10$, Length $l_p = 9.8$, $\mu_0 M = 0.1732T$	
Upper-ring PM : $d_o = 20, l_p = 2$.	
Three different types of PMs : $\mu_0 M$ (Location index)	
0.244T (1,5,9,10), 0.229T (2,4,8,12), 0.203T (3,6,7,11)	
MFD sensors ($N_s=11$): $h_s = 15, r_s = 38$	

Table 3. Spherical motor parameters (Dimension in mm).



The diagram illustrates the spherical motor's geometry. It shows a 3D coordinate system with axes X or x, Y or y, and Z or z. A rotor PM (Permanent Magnet) is shown as a red sphere with radius R, with angles ϕ_x and ϕ_z relative to the axes. The stator EM (Electromagnet) is shown as a cylindrical shell with outer radius a_o and inner radius a_i , and length l . The magnetic moment $M = M\hat{z}$ is indicated. The rotor PM is labeled with $N_P = 20$ and $\mu_0 M = 0.3464T$. The stator EM is labeled with $N_E = 24$, $R_e = (11 \pm 0.13) \Omega$ (800 turns, wire diameter = 0.32), $a_o = 18.75$, $a_i = 7.7$, and $l = 12$.

Rotor PM: $N_P = 20$, $\mu_0 M = 0.3464T$, $a_o = 19.7$, $l = 3.9$.				
<i>xyz</i> frame	Index, i^{th}	ϕ_x	ϕ_z	Polarity, λ
$R = 55$	1~10	70°	$36^\circ \times (i-0.5)$	$(-1)^i$
	11~20	110°	$36^\circ \times (i-10.5)$	$(-1)^{i-1}$
Stator EM: $N_E = 24$. $R_e = (11 \pm 0.13) \Omega$ (800 turns, wire diameter = 0.32) $a_o = 18.75$, $a_i = 7.7$, $l = 12$				
<i>XYZ</i> frame	Index, j^{th}	ϕ_x	ϕ_z	
$R = 44$	1 ~ 8	55°	$45^\circ \times (i-0.5)$	
	9 ~ 16	90°	$45^\circ \times (i-9)$	
	17~24	125°	$45^\circ \times (i-16.5)$	

To implement the sensing and control algorithms in real time, a combination of FPGA and real-time processing is accomplished using National Instrument's (NI) cRIO 9035. In addition, C series modules can be installed into the cRIO for signal measurement and signal output. Two NI 9205 voltage input modules can be used to collect the voltage of the 11 vertically aligned single axis MFD sensors (A1302) and the back-EMF of the 12 pairs of copper coils. The MFD sensors are supplied 5V by a Keithley 2231A power supply which then returns a voltage signal linearly proportional to the measured MFD. The NI 9264 voltage output module sends a voltage signal to an array of circuit boards that converts the voltage to an amplified current signal. The described embedded control system is shown in Figure (6d). It is found that the voltage to current relationship is not linear, so a simple integral controller is developed in LabVIEW to correct the voltage output signal to coerce measured current to a desired current. The measured current can be estimated by dividing the measured EMF by the coil's

resistance, assuming that inductive effects are small. The data collection modules and algorithm implementation can all be conveniently programmed using LabVIEW. Figure 7 shown below depicts the experimental setup in block diagram form.

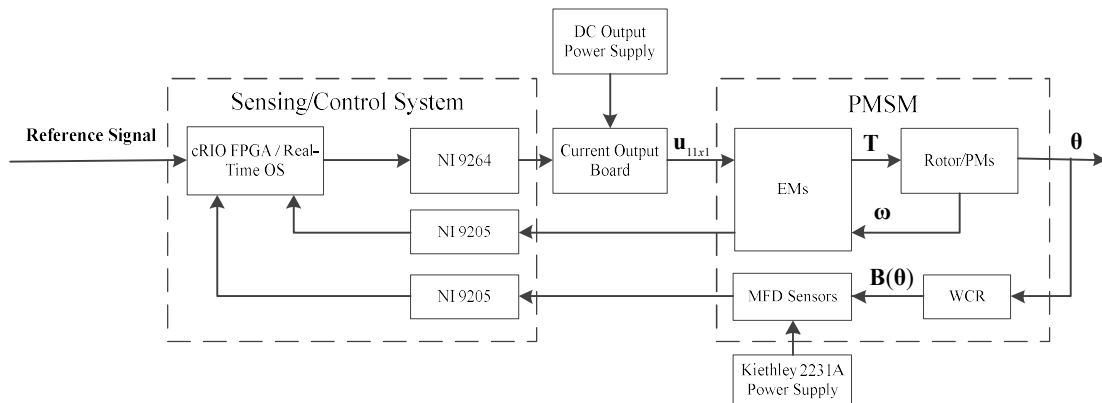


Fig. 7. System dataflow depicted in block diagram form.

In order to use the Kalman Filter sensing model, the ANN model needs to first be calibrated. This can be accomplished by collecting training data corresponding to the voltage array of the 11 MFD sensors for known orientations of the rotor. A calibration module is designed to automatically move the rotor to known orientations and collect MFD sensor readings. An image of the calibration module is shown on the following page in Figure (8a), and a flow chart of the data collection procedure in Figure (8b).

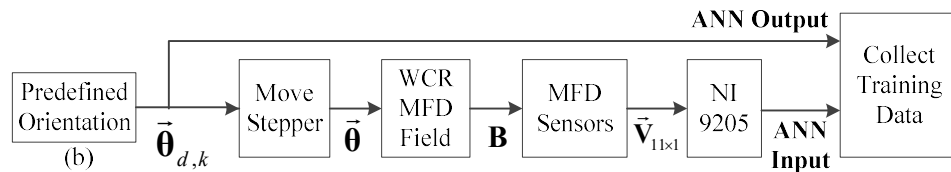
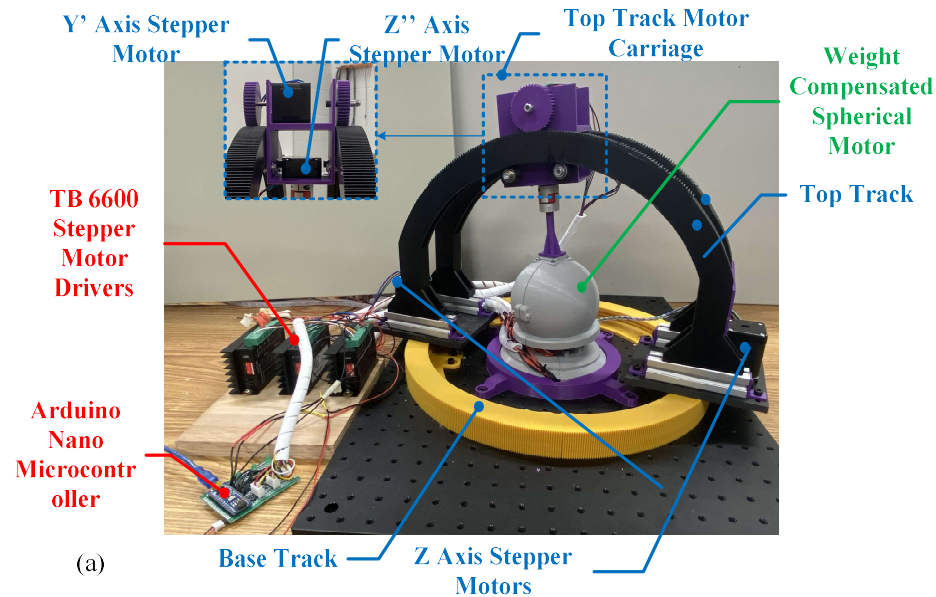


Fig. 8. ANN Calibration Module. (a) Module Setup, (b) Illustration of Calibration Module.

The calibration module operates as a spherical gantry system, consisting of a circular base track and two parallel half-circle top tracks. Each track has gear teeth on the outside surface and a double-v groove on its interior, allowing for the motor carriages to travel along them. Two motor carriages are attached on opposite ends of the base, and one is attached to the top tracks. The attachments are made by a pinion driven by a stepper motor meshed with the gears on the track and double-v wheels that roll along the groove of the interior of the tracks. These constraints force the carriages to move along the circular path of the tracks. The top track motor carriage has an additional idler pinion for the additional track, so that the carriage can sit evenly in between the two top tracks.

The top track has an additional stepper motor that directly connects to the stepper motor via shaft and shaft coupler.

The structure of the calibration module allows the for the rotor to be moved to known orientations as the gear ratios and the angle of the stepper motors are both known. The rotation can be pictured as “ZYZ” Euler angles, where the base carriage stepper motors drive the top track about the stator Z axis, the geared top carriage stepper rotates the rotor about its Y' axis, and the top carriage stepper directly connected to the rotor spins it about its Z'' axis.

A MATLAB program can be made to facilitate a calibration data collection routine, where the program sends commands to an Arduino Nano programmed to send the appropriate signals to the stepper motor drivers (TB 6600), and request MFD sensor voltage readings from an NI 9205 voltage input. Given that the gear ratios of the system are known, the inputs and outputs necessary to train the ANN for a given calibration range can be determined.

4.2 Sensing Experiment Results and Analysis

The accuracy and efficiency of the sensor fusion based on embedded magnetic sensing and back-EMF based measurements of the angular velocity are experimentally evaluated on the prototype testbed shown in Figures 6 (a, b).

As shown in Figure 9(a), the two laser-pointers are placed orthogonally at $(0, 0, R)$ described in the local xyz frame of the rotor (radius r_p). During initialization, the xyz frame is oriented to coincide with the stator XYZ frame. To achieve a resolution in the order of 0.005° , the two orthogonal laser beams are projected to two distance planes with

1cm² grids (Figure 8a); Planes 1 and 2 placed at ($X_1=371\text{cm}$, $Y_1=0$) and ($X_2=0$, $Y_2=392\text{cm}$), respectively.

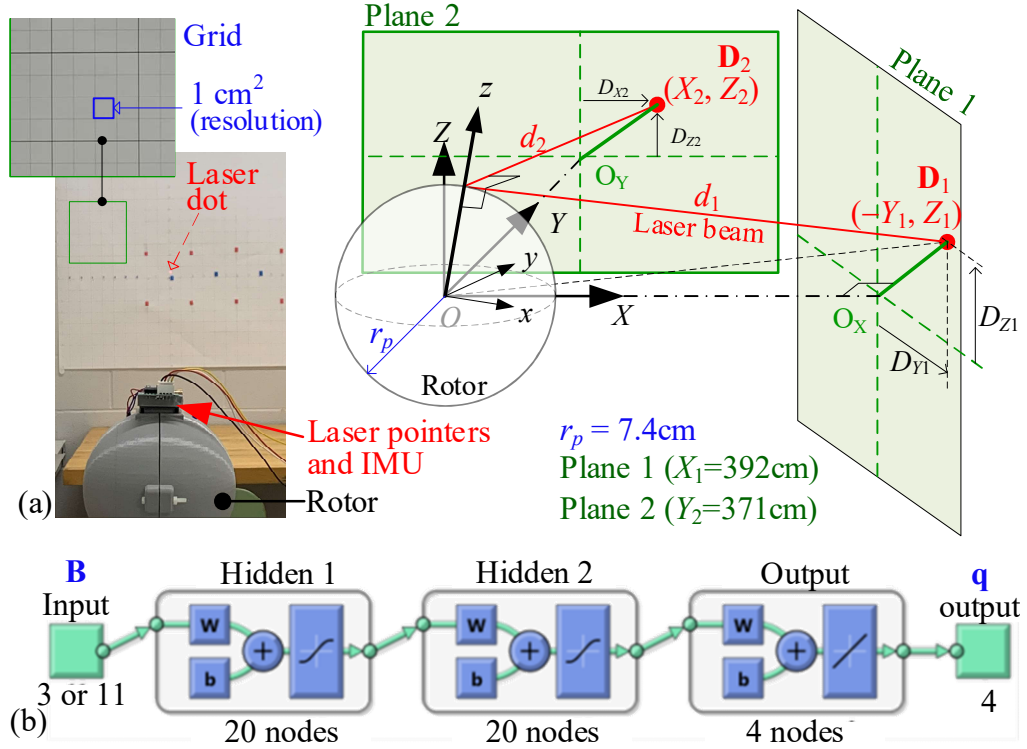


Fig. 9. Experimental ANN training. (a) Schematics illustrating the input-output data measurements. (b) ANN architecture.

At any given rotor orientation, the two beams that are parallel to the (x, y) axes are projected onto Planes (1, 2) as two dots (D_1, D_2); their position vectors with respect to the XYZ and xyz frames are given by (25a, b) where the perpendicular distances (d_1, d_2) from the (yz, xz) planes are given by (25c):

$$\mathbf{D}_1 = \begin{cases} = \mathbf{P}_1 = [X_1 & -Y_1 = D_{Y1} & Z_1 = D_{Z1}]^T |_{XYZ} \\ = \mathbf{p}_1 = [d_1 & 0 & r_p]^T |_{xyz} \end{cases} \quad (25a)$$

$$\mathbf{D}_2 = \begin{cases} = \mathbf{P}_2 = [X_2 = D_{X2} & Y_2 & Z_2 = D_{Z2}]^T |_{XYZ} \\ = \mathbf{p}_2 = [0 & d_2 & r_p]^T |_{xyz} \end{cases} \quad (25b)$$

$$\text{where } d_i = \sqrt{(X_i^2 + Y_i^2 + Z_i^2) - r_p^2}. \quad (25c)$$

Using the quaternion \mathbf{q} defined in (10) to describe the rotor orientation, the 3D projected points (\mathbf{D}_1 or \mathbf{D}_2) in the xyz frame can be expressed in the XYZ frame using (26) where (\mathbf{P}_{XYZ} , \mathbf{p}_{xyz}) are the position vector of the point in the (XYZ, xyz) frames:

$$\begin{bmatrix} 0 \\ \mathbf{P}_{XYZ} \end{bmatrix} = \mathbf{q} \otimes \begin{bmatrix} 0 \\ \mathbf{p}_{xyz} \end{bmatrix} \otimes \mathbf{q}^* \quad (26)$$

Along with the constraint $\|\mathbf{q}\|=1$, the quaternion \mathbf{q} can be calculated by simultaneously solving (26) for the pair of projected points (\mathbf{D}_1 and \mathbf{D}_2) for a specified rotor orientation using the Levenberg-Marquardt algorithm.

Three 4-output-ANN algorithms are designed to investigate the effects of sensor configurations on the measurements:

ANN-1 (3-input): Three adjacent sensors, S_1, S_2, S_3

ANN-2 (3-input): Three evenly spaced sensors, S_1, S_4, S_7

ANN-3 (11-input): Eleven evenly spaced sensors

Each ANN was trained with 725 input-output pairs. When collecting data for training an ANN, the two laser spots are positioned within the ranges of the two planes in the step of approximately 0.3° :

Plane 1: $D_{Y1}, D_{X2} \in [-10, 50]\text{mm}$ $\alpha \in [-2^\circ, 8^\circ]$

Plane 2: $D_{Z1}, D_{Z2} \in [-8, 8]\text{mm}$ $\beta, \gamma \in [-2^\circ, 2^\circ]$

As shown in Figure (6b) and Table 3, the stator-EMs are circumferentially distributed on three evenly spaced rings about the XY -plane with their magnetization axes passing through the stator center. Because of the symmetry, they are organized into

twelve pairs by series connections: for example, EM1-EM21 and EM9-EM13. In other words, $N_E/2=12$ independent channels are available for measuring the back-EMF to estimate the angular velocity ω with (9) where the orientation-dependent matrix $[\mathbf{G}]$ must be updated in real time. To improve the measurement bandwidth, $[\mathbf{G}]$ is precalculated and stored as a function of rotor orientation, where the individual magnetic flux linkage Λ_p between a PM and an EM is a function of the separation angle ϕ between them. For a given set of (PM, EM) design parameters summarized in Table 3, $f(\phi)$ defined in (5b) can be numerically calculated (Appendix) and curve-fitted, from which its derivative $f'(\phi)$ for \mathbf{G}_j in (7b) can be derived; the results are plotted in Figure 10.

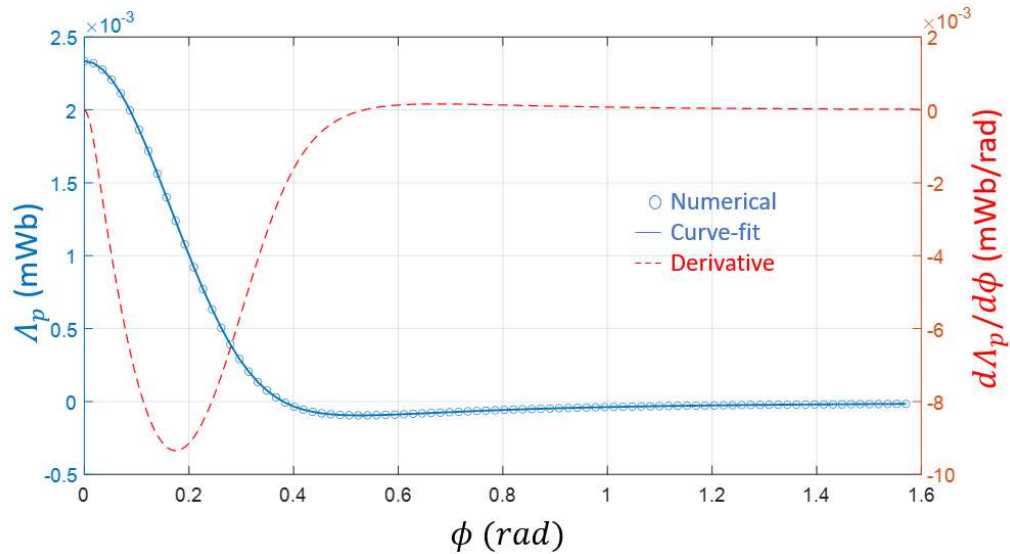


Fig. 10. Magnetic flux linkage function and its derivative.

The sensor-fusion method is experimentally evaluated, where the results are organized into two groups:

- ANN and KF estimated rotor-orientation (α, β, γ)

- Simultaneous estimation of the rotor orientation (α, β, γ) and angular velocity $(\omega_x, \omega_y, \omega_z)$.

As a basis for evaluation, the results are compared with those measured by the optical system (Fig. 9a) and by the commercial IMU (MPU6050).

The experimental results comparing the ANN-measured and KF-estimated Euler angles are presented in Figures 11(a, b) and Table 4 where eight optically measured data serve as ground truth to analyze the effects of different sensing methods on the mean and standard deviation (SD) of the orientation errors.

Table 4. Reference rotor orientations and relative errors.

Optically measured orientation (ground truth) for error evaluation							
Plane	$X_1=371$ (cm)		$Y_2=392$ (cm)		Euler (zyx) angles ($^\circ$)		
Point	D_{Y1}	D_{Z1}	D_{X2}	D_{Z2}	α	β	γ
1	8	4	7.6	0	1.110	0.012	-0.618
2		-4	7.8	4.8	1.140	0.680	0.632
3	16	4	16.7	-0.5	2.439	-0.049	-0.620
4		-4	15.4	1.2	2.249	0.151	0.624
5	24	4	25.0	0.5	3.648	0.112	-0.611
6		-4	24.8	2.5	3.618	0.326	0.638
7	32	4	33.3	-0.2	4.854	0.023	-0.616
8		-4	33.2	1.6	4.839	0.181	0.633
Orientation error ($^\circ$) relative to optically measured data:							
Rel. error	Mean			Standard deviation (SD)			
	α	β	γ	α	β	γ	
ANN-1	-0.832	0.431	0.414	1.015	0.306	0.683	
ANN-2	0.470	-0.212	-0.205	0.469	0.286	0.257	
ANN-3	-0.106	-0.014	-0.073	0.080	0.039	0.070	
KF	-0.090	0.001	-0.051	0.052	0.050	0.081	

As shown in Table 4 where the (mean, SD) errors are compared among the three different ANN-based sensing systems (ANN-1, 2, 3), the 11-input ANN-3 exhibits the best performance (where both the mean and SD of the errors are less than 0.1°) followed by the 3-input ANN-2. Although three single-axis MFD-sensors are sufficient to uniquely

estimate the rotor orientation, the (mean, SD) errors of ANN-2 are half of that of ANN-1 implying that sensor placement has an influential effect on measurement errors. The 11-input ANN-3, with its (mean, SD) errors nearly an order of magnitude lower than that of the 3-input ANN-1 and 2, is used in the subsequent studies.

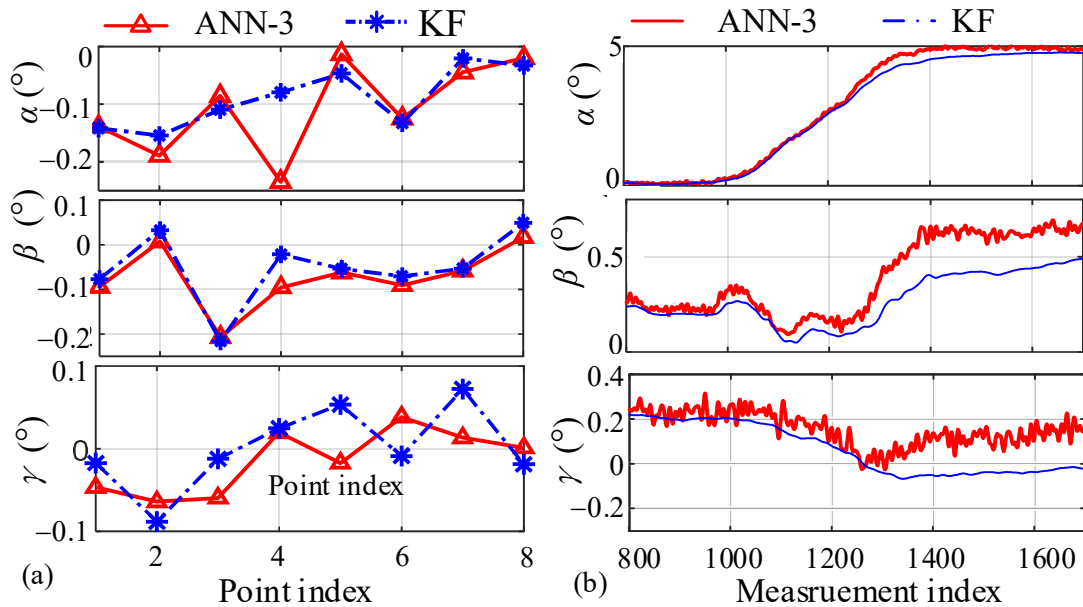


Fig. 11. Relative errors of ANN-measured and KF-estimated Euler angles. (a) Eight points in Table 4. (b) Arbitrary trajectory.

Experiments are conducted to analyze the effects of three different sensor-fusion methods on simultaneous estimation of the Euler angles and their angular velocities along an arbitrary orientation trajectory:

Method 1 (IMU): Euler angles are estimated using a complementary filter with acceleration and angular-velocity measurements [31].

Method 2 (ANN-3): Euler angles are estimated using ANN-3 with all MFD sensor measurements.

Method 3 (KF-based sensor fusion): Both Euler angles and their angular velocities are

simultaneously estimated using KF with the ANN-3 and EMF measurements.

The results are compared in Figure 12 and Table 5. The left column of Figure 12 compares the Euler angles estimated using IMU measurements, KF-based sensor fusion method and ANN-3 model whereas the right column compares the angular velocity measured/estimated by the IMU and the KF-based sensor fusion. The statistics of their differences between the results from IMU and the KF-based sensor fusion method are compared in Table 5.

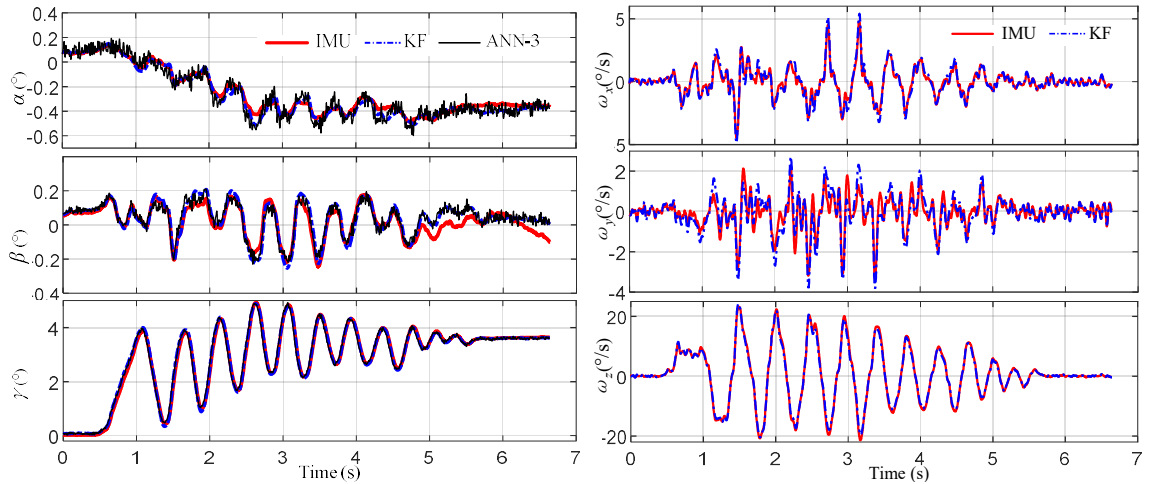


Fig. 12. KF and IMU comparison for orientation and angular velocity.

Table 5. Statistics of the orientation and angular velocity difference between KF estimation and IMU.

Difference	Orientation (°) (α , β , γ)	Angular velocity (°/s) (ω_x , ω_y , ω_z)
Mean	(0.0168, 0.0831, 0.0421)	(0.1520, -0.0143, -0.0025)
STD	(0.6572, 0.9368, 1.475)	(0.1856, 0.1523, 0.0825)

Shown in Figure 12, the ANN-3 and the KF display nearly identical estimations of the arbitrary orientation trajectory. However, as observed in Figure 11(b), ANN-3 data are noisy and hence cannot be used to derive the velocities from the first derivative of the

Euler angles. In contrast, the orientation trajectory data which are numerically integrated from the measured velocity, is smooth but suffers noticeable drift after 5 seconds when the rotor stops moving, especially the β angle.

As demonstrated in Figure 11, Figure 12, and Table 5, the KF- based sensor fusion with embedded MFD and EMF sensors effectively overcome the sensor noise and IMU drift problems and is capable of simultaneously estimating both the orientation and angular-velocity with improved accuracy and smaller SD than that of the popular IMU measurements.

4.3 Control Experimental Results and Analysis

The accuracy and effectiveness of the PMSM control scheme is tested and analyzed. Specifically, the system's ability to achieve regulation and tracking control are to be verified. The regulation control can be evaluated by providing a static orientation input to the SMC and comparing the orientation output of both sensor readings and ground truth measurements. Similarly, the tracking control can be evaluated by analyzing the response providing a dynamic orientation input.

The operating range of the experiments correspond to the orientation necessary such that the optical system in Figure 9(a) can point a laser within an 45cm x 15cm rectangular range on whose center is on Plane 2 placed at $(X_2=0, Y_2=117\text{cm})$ and the orthogonal laser can maintain a vertical range of ± 7.5 cm on Plane 1 $(X_1=117\text{cm}, Y_1=0)$. The range on Plane 2 is discretized into a 12 x 15 grid and the Plane 1 range is separated into 12 segments, which correspond to an array points representing \mathbf{D}_1 and \mathbf{D}_2 in (25).

(26) can then be solved for each point which providing corresponding rotor orientations that the calibration module is then used to train an ANN.

For each experiment, the control loop operates at 500 Hz. Multiple signals are filtered in real time using second order lowpass Butterworth filters with varying cutoff frequencies. The measured magnetic field, orientation derivative terms, calculated control law, and control signal are filtered with a cutoff frequency of 2, 5, 3, and 10 Hz.

4.3.1. Regulation Control

Four step inputs (θ_d) are tested the system response for each is analyzed for its ability to reach a desired point. The first three points are single-axis inputs corresponding to X , Y , and Z axis, where only the respective component of θ_d for each point is nonzero. The fourth point tested corresponds to a general case, where each component of θ_d is nonzero. Parameters including peak time, rise time, maximum overshoot, and steady state error can then be studied as a basis of performance metrics. The values of the proportional gains and the smoothing constant are tuned to optimize performance, where $[\mathbf{k}] = \text{diag}(50, 45, 18)$, $[\mathbf{P}] = (20, 45, 23)$ and $\Omega = 1.25$ for the following regulation experiments. The tests are performed and the results along with input parameters are depicted in Table 6. The recorded parameters include steady state value (SSV), steady state error (SSE), rise time (T_r), peak time (T_p), max overshoot (Max OS), settling time (T_s), and the steady state error band.

Table 6. Regulation Control Results

Point	$\theta_d(^{\circ})$	$SSV(^{\circ})$	$SSE(^{\circ})$	$T_r(sec)$	$T_p(sec)$	$Max OS(^{\circ})$	$T_s(sec)$	$T_s Band$
1	(-2.292, 0, 0)	-2.263	-0.029	0.131	0.164	-0.830	0.534	2%
2	(0, 2.292, 0)	2.327	-0.035	0.250	0.2698	0.168	0.307	2%
3	(0, 0, 2.865)	2.960	-0.095	0.272	0.364	1.325	0.426	5%
4	$\theta_x: -2.292$	-2.372	0.080	0.130	0.166	-1.032	0.562	2%
	$\theta_y: 1.719$	1.874	-0.155	0.176	0.406	0.261	0.434	5%
	$\theta_z: 2.865$	3.054	-0.189	0.144	0.172	1.043	0.555	5%

Analyzing the results of the single axis step inputs (points 1-3) shows that the largest steady state error is approximately 0.095° in magnitude corresponding to the Z-axis step and the smallest steady state error is approximately 0.029° corresponding to the X-axis step. Generally, the X-axis step performed the best as it resulted in the lowest steady state error, peak time, and rise time. The larger error in the Z-axis step could possibly be a result of unmodeled nonlinear torque effects from the WCR.

Comparing the single axis step results to multi-axis step results, the performance parameters of the X-axis remains relatively unchanged where the other axes show a slower time response and higher steady state error. Figure 13 compares the desired orientation and torque vs the measured in addition to the value of the sliding surface s for each axis component of the fourth point.

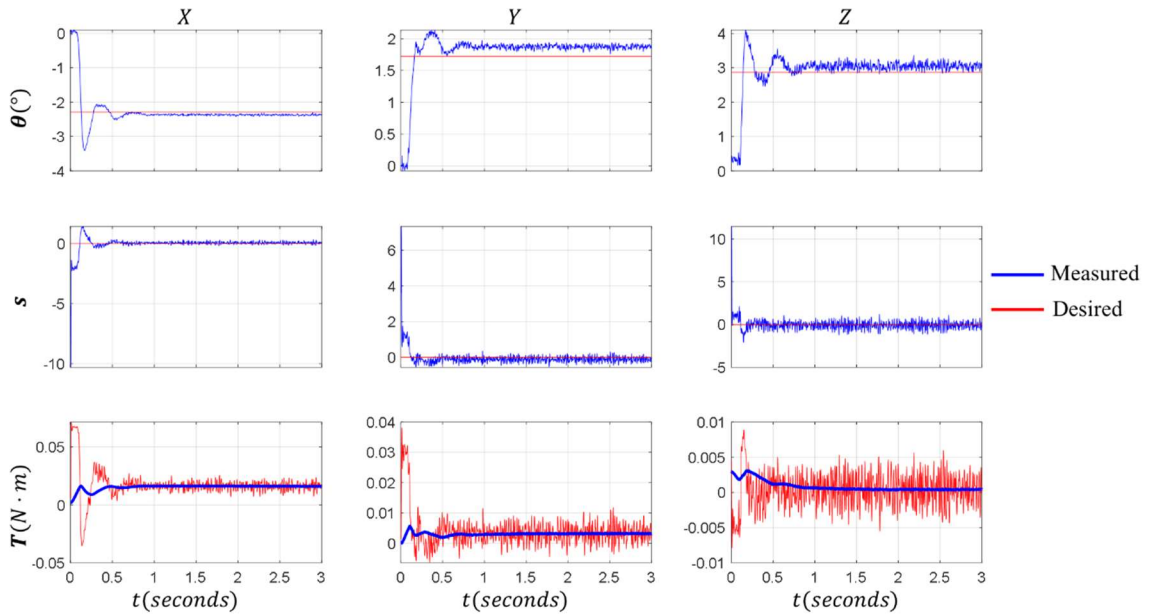


Fig. 13. Multi-Axis Regulation Control Results

It can be seen that the orientation response stabilizes near the desired value. The behavior of the sliding dynamics also validates the regulation control capabilities, as s can be seen to stabilize at 0. The convergence of the measured and desired torque signifies that the physical system is able to track the control law correctly. The noise apparent in the desired torque can be explained by the noise that propagates through orientation sensitive terms that are discretely derived in the desired control law in (21a, b).

The larger steady state error corresponding to the Y and Z axes could be explained by the selection $[k]$ and Ω , where decreasing Ω or increasing $[k]$ can reduce steady state error but also increases overshoot and reduces stability. When the smoothing constant is high or $[k]$ is small, less control effort will be applied when measured orientation is close to its desired value which could explain higher steady state errors. However, if Ω is too

small and $[k]$ is too large, oscillatory behavior is more likely which can lead to instability and more chatter. Similarly, larger values of $[P]$ are observed to improve response time reduce SSE but can lead to unstable behavior if chosen to be too large. As $[P]$ is multiplied by error terms in (18a, b), sharp discontinuities introduced by noise will have exaggerated effects on the control law. Therefore, the choosing of the control gains and smoothing constant should be tuned to minimize error and chatter while also avoiding unstable oscillatory behavior.

4.3.2 Tracking Control

The PMSM control system is then to be verified by analyzing the system's response to a dynamic input. Figure 14 depicts the results of the experiment, showing the individual axis components of the measured and desired orientation and torque in addition to the sliding dynamics for $[k] = \text{diag}(50, 45, 22)$, $[P] = (50, 40, 23)$ and $\Omega = 0.85$.

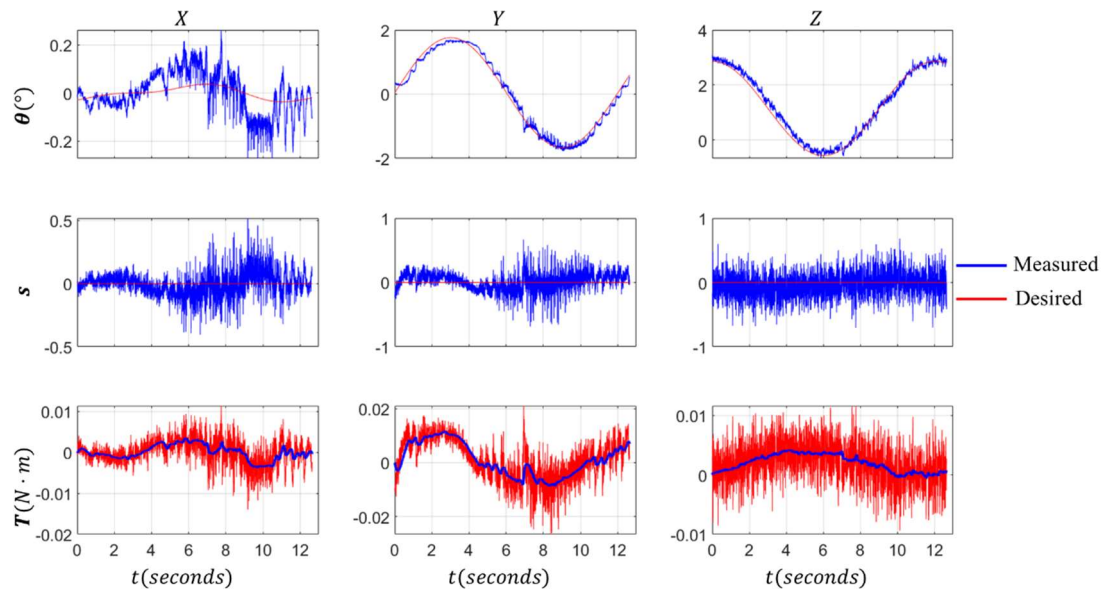


Fig. 14. Circular Trajectory Tracking Control Results

It can be seen that the measured orientation closely resembles the desired orientation for the Y and Z axis. A discrepancy in the X axis orientation curves could be explained as a sensitivity issue as the desired trajectory is near-zero. Observing the sliding dynamics indicate that \mathbf{s} is centered around $\mathbf{0}$, but with notable noise. The noise of the Z component of \mathbf{s} remains relatively constant, but a significant increase can be seen in the X and Y component around the 6 second mark. A noticeable increase in noise can also be seen in the X and Y component around the same time. As \mathbf{s} is directly correlated to orientation error and the corresponding derivative, the increase of noise in \mathbf{s} can be concluded to be a result of increased noise in measurements.

It is expected that the measurement noise is orientation dependent as a direct result of the sensitivity of the ANN sensing model. The accuracy of the ANN model is not constant throughout its domain, meaning some orientations will have higher uncertainties than others. These regions of higher error will propagate through $[\mathbf{K}_T]^{-1}$, as it is trained using an orientation dependent ANN which is subject to the same problem.

Chapter 5: Concluding Remarks and Future Work

The unique magnetic sensing system and a SMC algorithm is implemented in a PMSM design. The proposed sensing model is shown to solve the magnetic inverse problem, such that a bijective property can be established between MFD measurements and rotor orientation. From this, a KF sensor fusion algorithms combines angular velocity estimates from back-EMF measurements and orientation estimates from MFD measurements using an ANN. The sensing model is validated from experimental results showing that the orientation estimates closely resembling ground truth measurements collected from an optical system. A first order SMC algorithm is then applied to control the nonlinear system and experiments show that tracking and regulation control is achieved. These results are promising, and lead way to future improvements and research.

WCR Dynamic Effects

The dynamic effects of the WCR are modeled as a function of tilt angle, resulting in a corresponding torque along the respective axis. The experimental results suggest that the WCR also has a significant effect on the Z axis torque which is not included in the model. Reducing the size of unique magnets of the upper WCR ring could reduce this effect but would also decrease the signal-to-noise ratio of the ANN sensing component in addition to reducing the desired effectiveness of the WCR. Therefore, a more sophisticated model of $T_r(\theta)$ could be realized over the entire domain of the PMSM with consideration of all WCR elements using commercial simulation software.

The undesired effects of $T_r(\theta)$ on the Z axis could be reduced by increasing the

quantity of N_W WCR magnets. It is expected that this would decrease nonlinearities previously described as the magnetic torque for a given tilt angle would be more uniform varying spin angle.

It can be argued that the WCR can be eliminated from the PMSM system entirely. Removing the bottom layer of in an application where a PMSM is used in a robotic manipulator, the Z axis of the stator will likely not always be parallel to gravity, further complicating the WCR effects. The gravity compensation can be instead realized through additional control effort applied to the EMs, removing the need to model Z axis-nonlinearities from the WCR effects.

Calibration Module

The accuracy and precision of ANN orientation sensing model is directly correlated to the quality of data collected from the calibration module. Improvements to the design should be made such that the calibration module origin and the rotor origin are almost perfectly aligned. Also, a method to ensure that both the device and rotor start in the same position during every data collection sequence would improve the repeatability of data collection, allowing for data sets to be reused over time. A future iteration of the calibration module should be designed with high precision and tight geometrical tolerances, increasing the certainty that the true rotor orientation aligns with the expected orientation from the stepper motor gantry system. However, improvements in accuracy should not sacrifice the speed of data collection, as the amount of points required increases exponentially as the range of calibration is made larger. Therefore, the diameter of tracks can be made smaller in addition to increasing the gear ratios, minimizing the

distance and steps required to move to a desired orientation.

Higher-Order SMC

The effects of system performance when using a higher order SMC should be investigated. Although the complexity of calculating the control law would increase, it is expected that chatter would be reduced, and the convergence accuracy would increase. Also, PID gains can be implemented into the second order sliding surface which would allow for more parameters to tune desired performance.

References

- [1] K.-M. Lee, K. Bai, and J. Lim, "Dipole Models for Forward/Inverse Torque Computation of a Spherical Motor," *IEEE/ASME Transactions on Mechatronics*, vol. 14, pp. 46-54, Feb 2009.
- [2] F. William, E. Laithwaite, and L. Piggot, "Brushless Variable-Speed Induction Motors," in *Proc. IEE*, no. 2097U, pp. 102-118, 1956.
- [3] F. William, E. Laithwaite, and G. Eastham "Development of Design of Spherical Induction Motors," in *Proc. IEE*, no. 3036U, pp. 471-484, 1959.
- [4] E. Laithwaite, "Design of Spherical Motors," in *Electrical Times*, vol. 9, pp. 921-925, 1960.
- [5] Z. Zhou and K.-M Lee, "Real-time motion control of a multi-degree-of-freedom variable reluctance spherical motor," in *Proc. IEEE Int. Conf. on Robotics and Automation*, vol. 3, pp. 2859-2864, 1996
- [6] K.-M. Lee, R. Sosseh, and Z. Wei, "Effects of the torque model on the control of a VR spherical motor," in *Control Engineering Practice*, vol. 12, pp. 1437-1449, Nov. 2004.
- [7] K.-M. Lee, G. Vachtsevanos, and C. Kwan, "Development of a spherical stepper wrist motor," in *Proc. IEEE, Conf. on Robotics and Automation* vol. 1, pp. 267-272, 1988
- [8] K.-M. Lee and C. Kwan, "Design Concept Development of a Spherical Stepper for Robotic Applications," *IEEE Trans. on Robotics and Automation*, vol. 7, pp. 175-181, Feb 1991.
- [9] K.-M Lee, X. Wang, "Dynamic Modeling and Control of a Ball-Joint-Like Variable-Reluctance Spherical Motor," In *IEEE American Control Conf.* pp. 2463–2467, 1992.
- [10] R. L. Hollis, S. E. Salcudean, and A. P. Allan, "A six-degree-of-freedom magnetically levitated variable compliance fine motion wrist: Design, modeling and control," *IEEE Trans. on Robotics and Automation*, vol. 7, pp. 320-332, 1991.
- [11] K. Kaneko, I. Yamada, and K. Itao, "A Spherical DC Servo Motor with Three Degrees of Freedom," *ASME, Dynamic Systems, Measurement, and Control*, vol. 11, pp. 398-402, 1988.
- [12] T. Shigeki, G. Zhang, and M. Osamu, "Development of New Generation Spherical Ultrasonic Motor," in *1996 IEEE Int. Conf. on Robotics and Automation*, pp. 2871-2876, 1996.

- [13] T. Amano, T. Ishii, K. Nakamura, et al., "Ultrasonic actuator with multidegree of freedom using bending and longitudinal vibrations of a single stator," in *Proc. IEEE Ultrasonics Symp.*, pp. 667-670, 1998.
- [14] K.-M. Lee and D. Zhou, "A real-time optical sensor for simultaneous measurement of three-DOF motions," *IEEE/ASME Transactions on Mechatronics*, vol. 9, pp. 499-507, 2004.
- [15] H. Garner, M. Klement, and K.-M. Lee, "Design and Analysis of an Absolute Non-Contact Orientation Sensor for Wrist Motion Control," in *Proc. IEEE/ASME Int. Conf. on Advanced Intelligent Mechatronics*, 2001, pp. 69-74.
- [16] Z. Qian, Q. Wang, X. Guo, et al., "Research of orientation detection method for spherical motor and effect on PD control system based on machine vision," in Pages 2186–2191 2014 17th International Conference on Electrical Machines and Systems (ICEMS). IEEE. 2014.
- [17] H. Son, and K.-M. Lee, "Two-DOF magnetic orientation sensor using distributed multipole models for spherical wheel motor," *Mechatronics*, v. 21, n. 1, pp. 156-165, 2011.
- [18] K. Bai and K.-M. Lee, "Direct field-feedback control of a ball-joint-like permanent-magnet spherical motor," *IEEE/ASME trans. on Mechatronics*, v. 19, n. 3, pp. 975-986, 2014.
- [19] S. Foong, K.-M. Lee, and K. Bai, "Harnessing embedded magnetic fields for angular sensing with nanodegree accuracy," *IEEE/ASME transactions on mechatronics*, v. 17, n. 4, pp. 687-696, 2012.
- [20] K. Bai, K.-M. Lee, and J. Lu, "A magnetic flux model based method for detecting multi-DOF motion of a permanent magnet spherical motor," *Mechatronics*, v. 39, pp. 217-225, 2016.
- [21] J. Xu, Q. Wang, G. Li, R. Zhou, Y. Wen, L. Ju, and S. Zhou, "Sensorless posture detection of reluctance spherical motor based on mutual inductance voltage," *Applied Sciences*, v. 11, n. 8, pp. 3515, 2021.
- [22] F. Chai, L. Gan, and L. Chen, "A novel tiered type permanent magnet spherical motor and its rotor orientation measurement principle," *IEEE Access*, v.8, pp. 15303-15312, 2020.
- [23] J. Wang, G. Jewell, and D. Howe, "Design and control of a novel spherical permanent magnet actuator with three-DOF," *IEEE/ASME Trans. Mechatronics*, vol. 8, no. 4, pp. 457–468, Dec. 2003.

- [24] Y. Liang, I. M. Chen, C. K. Lim, et al., "Design and analysis of a permanent magnet spherical actuator," *IEEE/ASME Trans. Mechatronics*, vol. 13, no. 2, pp. 238–248, Apr. 2008.
- [25] H. Son and K.-M. Lee, "Distributed multipole models for design and control of PM actuators and sensors," *IEEE-ASME Trans. on Mechatronics*, vol. 13, pp. 228-238, Apr 2008.
- [26] C. Xia, C. Guo, and T. Shi, "A Neural-Network-Identifier and Fuzzy-Controller-Based Algorithm for Dynamic Decoupling Control of Permanent-Magnet Spherical Motor," *Industrial Electronics, IEEE Transactions on*, vol. 57, pp. 2868 - 2878, 2010.
- [27] Y. Zhao, S. Li, L. Zhao, et al., "Sliding-mode Control of Permanent Magnetic Spherical Motor based on Co-simulation Platform," in *IEEE 11th Conf. on Industrial Electronics and Applications*, pp. 119-123, 2016.
- [28] K. Bai, H Yan, K.-M. Lee, "Robust control of a spherical motor in a moving frame," *Mechatronics (Oxford)*, vol. 75, pp. 102548, 2021.
- [29] M. Li, and J. Ammanabrolu, "Indoor way-finding method using IMU and magnetic tensor sensor measurements for visually impaired users," *Int. J. of Intelligent Robotics and Applications*, v. 5, n. 2, pp. 264-282, 2021.
- [30] R. Kalman, "A new approach to linear filtering and prediction problems," *J. of Basic Engineering*, v. 82, pp. 35-45, 1960.
- [31] H. Fourati, "Heterogeneous data fusion algorithm for pedestrian navigation via foot-mounted inertial measurement unit and complementary filter," *IEEE Trans. on Instrumentation and Measurement*, v. 64, n. 1, pp. 221-229, 2015.
- [32] K. Bai, "Direct field-feedback control for permanent magnet spherical motors," Ph.D. dissertation, College of Mech. Eng., Georgia Inst. of Tech., 2012
- [33] J. D. Jackson, *Classical Electrodynamics*: New York: Wiley, 1999.

Appendix

Magnetic Flux Linkage Computation of a PM-EM Pair [20]

The magnetic flux linkage Λ_p contributed by a PM in the EM winding is a function of the separation angle φ (Fig. 1b). For an EM (volume V_E) that can be treated as a contiguous filamentary conductor (wire cross-sectional area a), Λ_p can be derived in terms of the vector potential \mathbf{A}_p generated by the PM from the volume integral (A.1) where the polarity λ ($= 1, -1$) denotes the sign of the PM magnetization and \mathbf{I} is the directional vector of the winding:

$$f(\varphi) = \frac{\Lambda_p}{\lambda} = \frac{1}{a\lambda} \int_{V_E} (\mathbf{A}_p \cdot \mathbf{I}) dv \quad (\text{A.1})$$

For a PM (magnetization \mathbf{M}) with a volume V_p bounded by surface area S_p , its vector potential \mathbf{A}_p at a point of interest can be computed from the sum of the volume and surface integrals in (A.2) where \mathbf{a}_n is the unit outward normal vector from ds and R is the distance from the source point to the point of interest:

$$\mathbf{A}_p = \frac{\mu_0}{4\pi} \left(\int_{V_E} \frac{\nabla \times \mathbf{M}}{R} dv + \int_{S_p} \frac{\mathbf{M} \times \mathbf{a}_n}{R} ds \right) \quad (\text{A.2})$$

Magnetic Flux Density Calculations for PMs and EMs

To understand the dynamics due to electromagnet effects, the various magnetic fields must be first quantified. From the Biot-Savart law [32], the vector quantity of \mathbf{B} produced at a point in space from an EM can be found using Equation (A.3), and the

vector quantity of \mathbf{B} produced at a point in space can be found from the negative gradient of the analytic magnetic potential [33] shown in Equation (A.4).

$$\mathbf{B}_{EM} = \frac{\mu_0}{4\pi} \int_V \frac{\mathbf{J} \times (\mathbf{R} - \mathbf{R}')}{|\mathbf{R} - \mathbf{R}'|^3} dV \quad (\text{A.3})$$

$$\mathbf{B}_{PM} = \frac{\mu_0}{4\pi} \int_V \frac{-(\nabla \cdot \mathbf{M})(\mathbf{R} - \mathbf{R}')}{|\mathbf{R} - \mathbf{R}'|^3} dV + \frac{\mu_0}{4\pi} \int_S \frac{-(\mathbf{M} \cdot \mathbf{n})(\mathbf{R} - \mathbf{R}')}{|\mathbf{R} - \mathbf{R}'|^3} dS \quad (\text{A.4})$$

Here, μ_0 is the permeability of free space, \mathbf{R} is the position vector of the field point, \mathbf{R}' is the position vector corresponding to the point of interest in which the MFD is calculated, $\mathbf{J}(= \frac{I}{A} \mathbf{n})$ is the current density at the field point, and \mathbf{M} is the magnetization vector of a PM.

Assuming the cylindrical PMs are uniformly axially magnetized, the first term in Equation (A.4) reduces to 0 and we are left with the surface integral term.

Magnetic Induced Force Calculations

The force created between interacting magnetic fields can be described using the Lorentz force equation shown below.

$$\mathbf{F}_m = - \oint \mathbf{B} \times I d\mathbf{n} \quad \text{where} \quad I = \oiint J dS \quad (\text{A.6})$$

Here, \mathbf{F}_m is the magnetic force created from the interaction between MFD \mathbf{B} with current I , which can be calculated as the equivalent surface current with surface element

dS and current density J . For a PM, the vector current density can be calculated to solve Equation (A.6) using the following expression.

$$\mathbf{J}_{PM} = \mathbf{a}_n \times \mathbf{M} \quad (\text{A.7})$$

Here, \mathbf{J}_{PM} is the vector current density, \mathbf{M} is the magnetization of a PM, and \mathbf{a}_n is the unit vector normal to the surface of a PM. As the PMs are axially magnetized, only the cylindrical surface of a PM will have an equivalent surface current.